JASA ARTICLE

Three-dimensional sound scattering from transversely symmetric surface waves in deep and shallow water using the equivalent source method

Tengjiao He,[1,a)] Victor F. Humphrey,[2] Shiqi Mo,[1,a),b)] and Erzheng Fang[1,a)]
[1]*College of Underwater Acoustic Engineering, Harbin Engineering University, Harbin, 150001, China*
[2]*Institute of Sound and Vibration Research, University of Southampton, Highfield, Southampton SO17 1BJ, United Kingdom*

ABSTRACT:
This paper proposes a propagation model to calculate the three-dimensional (3-D) sound scattering from transversely symmetric sea surface waves in both deep and shallow water using the equivalent source method (ESM). The 3-D sound field is calculated by integrating an assembly of two-dimensional (2-D) transformed fields with different out-of-plane wavenumbers through a cosine transform. Each 2-D solution is calculated using the ESM incorporating a complex image method that can efficiently and accurately solve the 2-D water/seabed Green's function. The oscillatory cosine integral is accurately calculated using a segmented integral scheme requiring relatively few 2-D solutions, which can be further improved through the use of parallel computation. The model is validated by comparison with a 3-D Helmholtz-Kirchhoff method for deep water and a finite element method for a shallow water wedge with both a fluid and an elastic seabed. The model is as accurate as the finite element approach but more numerically efficient, which enables Monte Carlo simulations to be performed for random rough surfaces in order to study the scattering effects at a reasonable computational cost. Also, 3-D pulse propagation in the shallow water wedge is demonstrated to understand the out-of-plane scattering effects further.
https://doi.org/10.1121/10.0001522

(Received 13 March 2020; revised 6 June 2020; accepted 17 June 2020; published online 8 July 2020)

[Editor: Steffen Marburg] Pages: 73–84

I. INTRODUCTION

Recent years have seen increased concern about the effects of man-made underwater noise on marine fauna. Due to the gradual increase of maritime traffic, underwater radiated noise (URN) emitted by vessels has become a major man-made contribution to ambient noise. This potentially poses a threat to marine fauna (Nowacek *et al.*, 2001; Lusseau *et al.*, 2009). In order to mitigate such man-made underwater noise, it is crucial to assess the URN from vessels. However, the precision and reliability of URN measurements for vessels can be strongly influenced by uncertainties related to the ocean environment (Mullor *et al.*, 2013). One of these uncertainties is the scattering effects owing to the rough sea surface that tend to play an important role in the frequency region above 1000 Hz (Audoly and Meyer, 2017).

In order to investigate and determine this uncertainty, an appropriate propagation model is required. Since the propagation range of interest for URN measurements is relatively short (Rodríguez *et al.*, 2015), the model needs to be accurate at short ranges. Additionally, the frequency range of interest from 10 Hz to 10 kHz implies the model should be numerically efficient. Rough surfaces have been considered in many two-dimensional (2-D) propagation models by assuming that the environment is axisymmetric (Collins *et al.*, 1995; Rosenberg, 1999; Thorsos *et al.*, 2004). However, the out-of-plane scattering is not included in these 2-D models, which means these models are unrealistic. To deal with more realistic scenarios, a three-dimensional (3-D) propagation model is needed, enabled by an approximate normal mode/parabolic equation hybrid model (Ballard, 2013; Ballard *et al.*, 2015). A study related to such a 3-D propagation model under a rough surface was carried out by Ballard (2013), showing that 3-D effects are essential in the direction perpendicular to the wind forcing. Although the energy scattered out-of-plane can be taken into account in this model, the azimuthal mode coupling is still absent, and the multiple-scattering is ignored. In addition, small range and azimuthal step sizes are required in order to obtain a good convergence for suddenly changing environments (such as a surface with large gradient) or for high frequencies, intensifying the computational load required to implement the model.

Apart from these classic models, the finite element method (FEM) has been extensively used for underwater acoustics (Isakson and Chotiros, 2011, 2014; Isakson *et al.*, 2014; Simon *et al.*, 2018). The advantage of the FEM is that it offers a full-wave solution containing all order scattering, even at a fairly short propagation range. Unfortunately, the

[a)]Also at: Key Laboratory of Marine Information Acquisition and Security (Harbin Engineering University), Ministry of Industry and Information Technology, Harbin 150001, China.
[b)]Electronic mail: moshiqi@hrbeu.edu.cn

FEM is numerically expensive, making a fully 3-D FEM solution impractical. However, a single-direction surface wave assumption can be made when studying the effect of surface scattering on URN measurements. Such an assumption provides a good approximation to the situation when the water surface waves have a relatively narrow angular spectrum so that the waves have a large correlation length in the transverse direction. Studies under the same assumption can be found in some 3-D propagation models associated with surfaces composed of straight sinusoidal waveforms (Welton, 2012; Smith, 2012; Choo *et al.*, 2016). Based on this assumption, the 3-D FEM solution can be obtained through the integration of a set of 2-D solutions owing to the transversely symmetric environment (Isakson *et al.*, 2014). Although the computational efficiency is improved by transforming the 3-D Helmholtz equation into 2-D, this model is suitable for a single implementation rather than for the multiple implementations required to investigate rough scattering. Repeatedly performing meshing and roughness realisations make this model time-consuming. Furthermore, a very large digital data storage space is required to save each component of the FE solutions, and the computational load increases rapidly as the frequency increases.

This paper proposes an equivalent source method-based transversely symmetric propagation model (ESM-TSM) to calculate the 3-D sound scattering from transversely symmetric sea surface waves in both deep water with no seabed reflections and in shallow water. The ESM-TSM assumes that the water surface waves only vary in one direction, and the seabed is allowed to slope in the same direction. A set of 2-D components corresponding to different out-of-plane wavenumbers are efficiently calculated by the ESM in parallel and then integrated through a cosine transform to obtain the 3-D field. In each 2-D solution, the sound field is the superposition of the incident field generated by the source plus the scattering field generated by a set of equivalent sources above the sea surface. The unknown strengths of the equivalent sources are then obtained by solving the inverse problem based on the boundary condition on the sea surface. For the case of shallow water, a complex image method (Fawcett, 2000) is used to calculate the water/seabed Green's function accurately. The oscillatory cosine integral is treated through a segmented integral based on the fast construction of the Clenshaw-Curtis Quadrature rules (Waldvogel, 2006) to achieve a good convergence using fewer 2-D solutions. The ESM-TSM has similar accuracy to the FEM, and the sea surface can be arbitrarily rough. Besides, an acceptable computational cost is needed to perform the multiple implementations required for studying the surface scattering since arbitrary field points can be calculated once the strengths of equivalent sources are determined. The ESM-TSM has been validated in this paper by comparisons with a 3-D Helmholtz integral method for the case of deep water and a FE model for the case of a shallow water wedge with both a fluid and an elastic seabed. The parameter selection for the segmented integral scheme is discussed, and a 3-D pulse propagation is demonstrated to understand the out-of-plane scattering effect further. The paper is organised as follows: Sec. II presents the formulae of the ESM-TSM, while Sec. III presents numerical results and discussions. Finally, the conclusion will be presented in Sec. IV.

II. AN EQUIVALENT SOURCE METHOD-BASED TRANSVERSELY SYMMETRIC PROPAGATION MODEL

The key aspect of the transversely symmetric propagation model approach taken is that 3-D field of a monopole source is modelled by considering an integral over a number of 2-D transformed fields for which the source will be a line source. For this, the waveguide geometry depends on the $x-$ and $z-$ directions. The ESM-TSM is easy to implement numerically compared with the Helmholtz integral method since it avoids the integrable singularity (Koopmann *et al.*, 1989). Also, the computational efficiency is higher than the FE model when large scale models or Monte Carlo simulations are required owing to the avoidance of repeat meshing. Furthermore, the surface roughness can be arbitrary in this model. The implementation of the ESM-TSM can be split into two steps: first the 2-D transformed scattering fields for different out-of-plane wavenumbers are calculated using the ESM, and then the 3-D scattering field is obtained through a cosine transform.

A. Two-dimensional transformed field based on the equivalent source method

As shown in Fig. 1, a line source is submerged in the ocean with a randomly rough surface waves. The water column is iso-velocity with a sound speed of c_1 and density of ρ_1. The 2-D field in water can be considered as the incident field generated by the line source plus the scattered field that is the superposition of N equivalent line sources above the location of the rough surface. The incident field on the rough surface, generated by the line source, is given by

$$p_{inc2D}(\boldsymbol{r}_\Gamma, \boldsymbol{r}_s|k_y) = 4\pi G(\boldsymbol{r}_\Gamma, \boldsymbol{r}_s|k_y), \quad (1)$$

where $\boldsymbol{r}_s$ and $\boldsymbol{r}_\Gamma$ are the position vectors of the source and the point on the 1-D rough surface and $G(\boldsymbol{r}_\Gamma, \boldsymbol{r}_s|k_y)$ is the 2-D Green's function at the field point $\boldsymbol{r}_\Gamma$ for an out-of-plane wavenumber k_y. For the case of deep water where the reflection from the seabed can be ignored, the 2-D Green's function is given by

$$G(\boldsymbol{r}_\Gamma, \boldsymbol{r}_s|k_y) = \frac{i}{4} H_0^{(1)}(k_{2D}|\boldsymbol{r}_\Gamma - \boldsymbol{r}_s|), \quad (2)$$

where $H_0^{(1)}$ is the first-class Hankel function of zero-order and $k_{2D} = \sqrt{(k_1^2 - k_y^2)}$ is the 2-D transformed wavenumber in water with $k_1 = \omega/c_1$, where ω is the angular frequency. Similarly, the scattered field on the rough surface can be written as

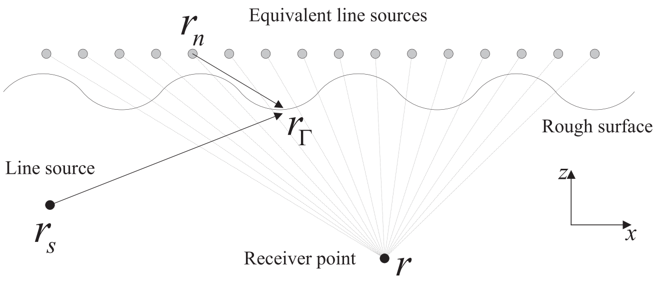

FIG. 1. The scheme of the equivalent source method for a 2-D rough surface in a deep water environment.

$$p_{s2D}(\boldsymbol{r}_\Gamma, \boldsymbol{r}_s|k_y) = \sum_{n=1}^{N} u_n G(\boldsymbol{r}_\Gamma, \boldsymbol{r}_n|k_y), \tag{3}$$

where $\boldsymbol{r}_n$ and u_n are the position vector and the strength of the nth equivalent source.

The incident and scattered field satisfy the boundary condition on the rough surface,

$$p_{inc2D}(\boldsymbol{r}_\Gamma, \boldsymbol{r}_s|k_y) + p_{s2D}(\boldsymbol{r}_\Gamma, \boldsymbol{r}_s|k_y) = 0. \tag{4}$$

Consider M points on the rough surface, Eq. (4) then can be written in matrix form as

$$\boldsymbol{GU} = -\boldsymbol{P}, \tag{5}$$

where $\boldsymbol{G}$, the $M \times N$ transfer matrix of the scattered field, has the form of

$$\boldsymbol{G} = \begin{pmatrix} G(\boldsymbol{r}_{\Gamma 1}, \boldsymbol{r}_1|k_y) & G(\boldsymbol{r}_{\Gamma 1}, \boldsymbol{r}_2|k_y) & \cdots & G(\boldsymbol{r}_{\Gamma 1}, \boldsymbol{r}_N|k_y) \\ G(\boldsymbol{r}_{\Gamma 2}, \boldsymbol{r}_1|k_y) & G(\boldsymbol{r}_{\Gamma 2}, \boldsymbol{r}_2|k_y) & \cdots & G(\boldsymbol{r}_{\Gamma 2}, \boldsymbol{r}_N|k_y) \\ \vdots & \vdots & \ddots & \vdots \\ G(\boldsymbol{r}_{\Gamma M}, \boldsymbol{r}_1|k_y) & G(\boldsymbol{r}_{\Gamma M}, \boldsymbol{r}_2|k_y) & \cdots & G(\boldsymbol{r}_{\Gamma M}, \boldsymbol{r}_N|k_y) \end{pmatrix}, \tag{6}$$

where $r_{\Gamma m}$ $(m = 1, 2, \ldots, M)$ is the position of the mth point on the rough surface, $\boldsymbol{U}$ is a $N \times 1$ unknown source strength vector and $\boldsymbol{P}$ is the pressure vector for the incident field on the 1-D rough surface with the size of $M \times 1$. By solving the inverse problem of Eq. (5), the unknown source strength vector can be obtained. In order to solve the inversion of matrix $\boldsymbol{G}$, sufficient samplings of the pressure on the rough surface are required. In this work, the number of equivalent sources was set to be the same as the pressure samples, which means that the exact solution for the source strengths could be efficiently determined by using the matrix division function in MATLAB. Otherwise, Tikhonov (Golub *et al.*, 1999) or other regularisation methods (Pereira *et al.*, 2015) need to be used when the number of equivalent sources is not equal to the number of pressure samples. The default equivalent source configuration was set to be a conformal line one-quarter-acoustic wavelength above the rough surface with five sources per acoustic wavelength unless specified. This assures the accuracy of the ESM since the spatial Nyquist criterion (Holland and Nelson, 2013) is satisfied. A detailed discussion of the influence of N on the accuracy can be found in Appendix A.

Thus, the 2-D scattered field at $\boldsymbol{r}$ in water can be calculated by

$$p_{s2D}(\boldsymbol{r}, \boldsymbol{r}_s|k_y)_{2D} = \sum_{n=1}^{N} u_n G(\boldsymbol{r}, \boldsymbol{r}_n|k_y). \tag{7}$$

B. 2-D half-space Green's function for the shallow water case

For the case of shallow water, the Green's function needs to be replaced by that for a half-space with two homogeneous layers. The method of complex images (Fawcett, 2000) is employed to calculate such a half-space Green's function, which has been used widely in electromagnetics (Yang and Chow, 1991) and underwater acoustics (Fawcett, 2003). The advantage of the complex image method is that once the amplitudes and complex positions of images are determined for a zero value of k_y, the Green's function for arbitrary k_y can be obtained using these image configurations. In addition, only a few orders of complex images can provide good convergence, which is numerically efficient.

Here, the seabed is allowed to slope in the same direction as the surface variation. Consider a two-layer half-space shown in Fig. 2. The water/seabed interface is assumed to be sloped with a slope angle θ. A new coordinate system (x', z') is introduced by rotating the original coordinate (x, z) by θ (Deane and Buckingham, 1993), where

$$\begin{cases} x' = \dfrac{x}{\cos\theta} + (z - x\tan\theta)\sin\theta, \\ z' = (z - x\tan\theta)\cos\theta, \end{cases} \tag{8}$$

with the water/seabed interface defined as $z' = 0$. Based on the complex image method, the Green's function for a field point (x'_r, z'_r) due to a line source at (x'_s, z'_s) above the

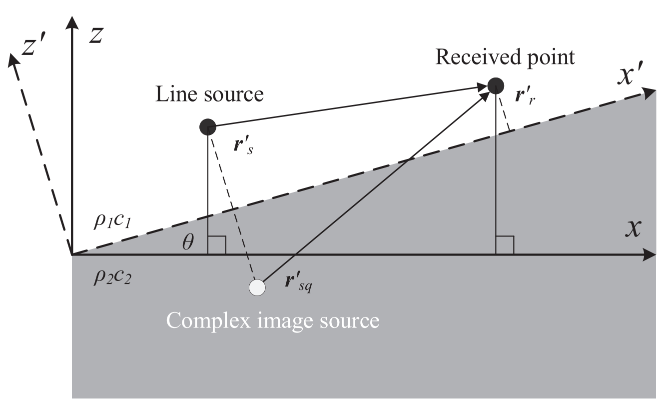

FIG. 2. The rotated coordinate system for the two-layer space with a sloping interference.

half-space can be represented as the wavenumber integral expression

$$G(\boldsymbol{r}'_r,\boldsymbol{r}'_s) = \frac{i}{4}H_0^{(1)}(k_1|\boldsymbol{r}'_r - \boldsymbol{r}'_s|) + \frac{1}{\pi}\int_0^\infty R(h)\frac{e^{i\gamma_1(z'_r+z'_s)}}{2i\gamma_1}\cos\left(h|x'_r - x'_s|\right)dh, \tag{9}$$

where $\boldsymbol{r}'_r$, $\boldsymbol{r}'_s$ are the position vectors of the receiver and source, and $|\boldsymbol{r}'_r - \boldsymbol{r}'_s| = \sqrt{(x'_r - x'_s)^2 + (z'_r - z'_s)^2}$. Here, h is the horizontal wavenumber, $\gamma_1(h) = \sqrt{(k_1^2 - h^2)}$ is the vertical wavenumber in water, and $R(h)$ is the water/sea interface reflection coefficient given by

$$R(h) = \frac{\rho_2\Psi(h)\gamma_1(h) - \rho_1\gamma_2(h)}{\rho_2\Psi(h)\gamma_1(h) + \rho_1\gamma_2(h)}, \tag{10}$$

where ρ_2 is the density of the seabed and $\gamma_2(h) = \sqrt{(k_2^2 - h^2)}$ is the vertical wavenumber in the seabed with $k_2 = \omega/c_2$ and a sound speed of the seabed c_2. For a fluid seabed $\Psi(h) \equiv 1$. For an elastic seabed, $\Psi(h)$ is given by (Fawcett, 2000)

$$\Psi(h) = (1 - 2h^2/\beta)^2 + 4\gamma_2(h)h^2\gamma_s(h)/\beta^2, \tag{11}$$

where $\beta = (\omega/c_s)^2$ and $\gamma_s(h) = \sqrt{(\beta - h^2)}$ is the shear vertical wavenumber in the seabed with a shear speed c_s.

The integral in Eq. (9) represents the reflected field in the upper half-space. The field generated by a line source at (x'_q, z'_q) can also be written as the wavenumber integral expression

$$\frac{i}{4}H_0^{(1)}(k_1|\boldsymbol{r}'_r - \boldsymbol{r}'_q|) = \frac{1}{\pi}\int_0^\infty \frac{e^{i\gamma_1(z'_r - z'_q)}}{2i\gamma_1}\cos\left(h|x'_r - x'_q|\right)dh. \tag{12}$$

Consider $z'_q = -z'_s + i\alpha_q$ and $x'_q = x'_s$, and the field generated by Q such line sources, then it follows that

$$\sum_{q=0}^{Q} a_q\frac{i}{4}H_0^{(1)}(k_1|\boldsymbol{r}'_r - \boldsymbol{r}'_q|) = \frac{1}{\pi}\int_0^\infty\left[\sum_{q=0}^{Q} a_q e^{\gamma_1\alpha_q}\right]\frac{e^{i\gamma_1(z'_r+z'_s)}}{2i\gamma_1}\cos\left(h|x'_r - x'_q|\right)dh, \tag{13}$$

where a_q is the amplitude of each source. If the parameters a_q and α_q are determined by

$$\sum_{q=0}^{Q} a_q e^{\gamma_1(h)\alpha_q} \approx R(h), \tag{14}$$

the reflected field in Eq. (9) then can be replaced by

$$G_r(\boldsymbol{r}'_r,\boldsymbol{r}'_s) = \sum_{q=0}^{Q} a_q\frac{i}{4}H_0^{(1)}(k_1|\boldsymbol{r}'_r - \boldsymbol{r}'_{sq}|), \tag{15}$$

where $\boldsymbol{r}'_{sq}$ is the position vector of the complex image and $|\boldsymbol{r}'_r - \boldsymbol{r}'_{sq}| = \sqrt{(x'_r - x'_s)^2 + (z'_r + z'_s - i\alpha_q)^2}$. The exponential fit can be solved by a Levenberg-Marquard method based on Eq. (14). In order to correct the singular behaviour of the Green's function for source and receiver points near the seabed, the asymptotic term with the singularity in the $R(h)$ should be removed while performing the fit using Eq. (14). For a fluid sea bed, only one asymptotic term $R_\infty = (\rho_2 - \rho_1)/(\rho_2 + \rho_1)$ should be subtracted. For an elastic seabed, $R_\infty = 1$ and one additional singularity corresponding to the Scholte wave should be removed. Here, the exponential fit for an elastic seabed follows a two-step procedure proposed by Fawcett (2000). First, the Scholte pole is determined by a Newton root-finding method for the zero denominator of Eq. (10), and then the parameters of exponential terms can be determined by fitting the reflection coefficient with only R_∞ subtracted. The exponential fit is implemented through a weighted fit giving less weighting when h approaches the Scholte pole. Due to the subtraction of the Scholte pole, the residue at this pole should be taken into account. However, this term, which represents the Scholte wave propagating mainly along with the interface, is only significant when both the source and receiver approach the water/seabed interface and therefore is neglected in this paper.

Once the amplitudes and complex positions of images are determined for k_1 ($k_y = 0$), the half-space Green's function for arbitrary out-of-plane wavenumbers k_y can be given by

$$G(\boldsymbol{r}'_r,\boldsymbol{r}'_s|k_y) = \frac{i}{4}\left[H_0^{(1)}(k_{2D}|\boldsymbol{r}'_r - \boldsymbol{r}'_s|) + \sum_{q=0}^{Q} a_q H_0^{(1)}(k_{2D}|\boldsymbol{r}'_r - \boldsymbol{r}'_{sq}|)\right], \tag{16}$$

where $a_0 = R_\infty$ and $\alpha_0 = 0$. For a general fluid seabed, 4 exponentials are sufficient to fit their reflection coefficient (Fawcett, 2000). However, for the elastic seabed, more terms are needed particularly when the shear speed is large. Therefore, six exponentials are used to calculate the half-space Green's function through Eq. (16) in this paper.

C. Three-dimensional solution of the scattered field

When the 2-D rough surface only depends on x, the 3-D scattering field for a point source can be calculated by integrating the 2-D transformed scattered field using the integral

$$p_{s3D}(x,y,z) = \int_0^{k_{ymax}} p_{s2D}(\boldsymbol{r}(x,z),\boldsymbol{r}_s|k_y)\cos(k_y y)dk_y, \tag{17}$$

where k_{ymax} is the maximum of the out-of-plane wavenumbers that is chosen as 1.2 times k. Clearly, the integral in Eq. (17) has an oscillatory nature, especially for a non-zero transverse range y. Isakson *et al.* (2014) proposed a discretization scheme in k_y based on a slightly offset gamma cumulative distribution function (CDF) to evaluate the integral. The CDF discretization gives finer sampling where the kernel is highly oscillatory, so a robust result can be achieved efficiently. However, when a non-zero transverse range y is considered, the $\cos(k_y y)$ term becomes oscillatory, which still requires an impractical number of sampling points for the CDF discretization. A segmented integral scheme that combines the CDF discretization and the fast construction of the Clenshaw-Curits Quadrature rules (Waldvogel, 2006) is used alternatively to calculate the integral in this paper. First, the CDF discretization scheme is used to divide the integral into p subintervals, which enables smaller subintervals for the region where the kernel is more highly oscillatory,

$$\int_0^{k_{ymax}} (\bullet) = \int_0^{b_1} (\bullet)_{CDF} + \int_{b_1}^{b_2} (\bullet)_{CDF} + \cdots \int_{b_{p-1}}^{k_{ymax}} (\bullet)_{CDF}. \tag{18}$$

Then, the variables k_y need to be discretized based on quadrature nodes within each subinterval $[b_j, b_{j+1}]$ $(j = 0, 1, \ldots, p-1)$,

$$k_{yi} = \frac{(t_i + 1)(b_{j+1} - b_j)}{2} + b_j, \tag{19}$$

where t_i is the quadrature node on the interval $[-1, 1]$,

$$t_i = \cos\vartheta_i, \vartheta_i = i\frac{\pi}{l}, i = 0, 1, \ldots, l. \tag{20}$$

The sub-integral then can be transformed into a quadrature weighted sum

$$\int_{b_j}^{b_{j+1}} (\bullet)_{CDF} = \frac{b_{j+1} - b_j}{2} \sum_{i=0}^{l} w_i p_{s2D}(\boldsymbol{r}(x,z), \boldsymbol{r}_s | k_{yi}) \cos(k_{yi} y), \tag{21}$$

where w_i are the quadrature weights that can be calculated using the fast Fourier transform as shown by Waldvogel (2006). In addition, by solving for the 2-D transformed fields in parallel, the numerical efficiency can be further improved. This can be implemented using the *parfor* command of the MATLAB parallel computing toolbox.

III. NUMERICAL RESULTS AND DISCUSSION

A. Three-dimensional scattered field in deep water

First, the ESM-TSM was validated for a deep water environment to check the out-of-plane scattering effects by comparison with a 3-D Helmholtz-Kirchhoff method. Here, the 3-D reflection from a corrugated surface wave was considered. All the simulation parameters were the same as in the work of Choo *et al.* (2016), with a source placed at a depth of 20 m for a frequency of 20 kHz. The sound speed in the water was 1500 m/s. The wave height and wavelength of the corrugated surface were 1.5 and 40 m, respectively. In the work of Choo *et al.* (2016), the 3-D sound reflection is observed owing to out-of-plane scattering from the longitudinal variation sea surface. This can be demonstrated through the focusing and caustic patterns observed in an oblique plane from x-axis with an azimuth angle of 45°. In our case, the scattered field in the same oblique plane was calculated. 18 000 2-D transformed fields were evaluated to perform the ESM-TSM. The local section of the scattered field from the depth of 0 to 30 m was calculated by the ESM-TSM, and it can be seen in Fig. 3(a) that similar focusing and caustic patterns arise. The excellent agreement of the scattered fields obtained by the two approaches can also be seen in Fig. 3(b) where the pressure level for a receiver depth of 20 m is shown as a function of range, thus demonstrating that the out-of-plane scattering is captured accurately by the ESM-TSM. Here, it should be noticed that the 3-D Helmholtz-Kirchhoff method is numerically efficient for the high-frequency problem since it utilises the analytical free-space Green's function and the stationary phase approximation. This approach is suitable for deep water. Furthermore, the accuracy of the low-frequency problem cannot be guaranteed because of the violation of the Kirchhoff approximation. Although more computational load is required to handle a high-frequency problem, the proposed model is accurate in any frequency region. In addition, the proposed model can be extended to shallow water.

B. Three-dimensional scattered field in a shallow water wedge

1. Parameters set-up

A shallow water wedge, as shown in Fig. 4(a), was then considered with both a fluid and an elastic seabed. The simulation parameters are given in Table I. The 2-D

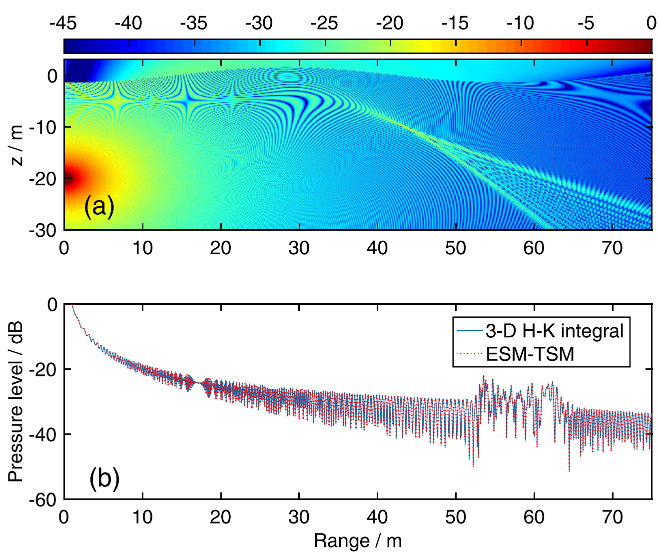

FIG. 3. (Color online) (a) The section of the sound field pressure level (in dB), for depths up 30 m, in an oblique plane with an azimuth angle of 45° to the x-axis. (b) Comparison of the scattered fields from corrugated surface waves calculated by the 3-D Helmholtz-Kirchhoff method and ESM-TSM in the same oblique plane for a receiver depth of 20 m.

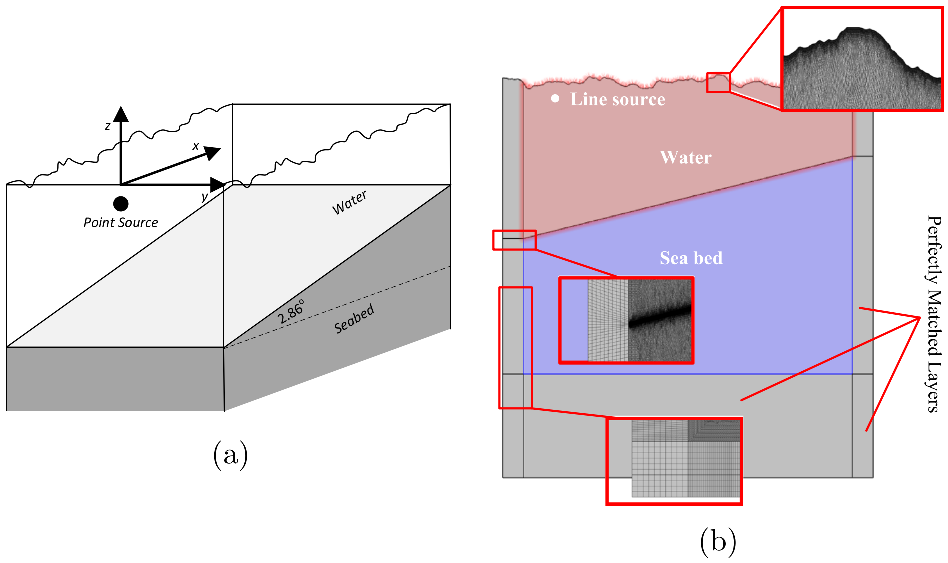

FIG. 4. (Color online) (a) The diagram of the shallow water wedge under transversely symmetric waves and with a sloping seabed angle of 2.86°. (b) The geometry for the 2-D FE model of the shallow water wedge with subplots displaying details of meshes of the sea surface, seabed boundary and the perfectly matched layer.

transversely symmetric sea surface was characterised by the Pierson/Moskowitz spectrum (Thorsos, 1990), which has a root mean square wave height of 2.13 m (Thorsos, 1990) and a correlation length of approximately 100 m for the default wind speed of 20 m/s used in the simulations. A longitudinally invariant finite element (LIFE) model (Isakson *et al.*, 2014) was adopted here as a benchmark. The 3-D solution was obtained by integrating over 2-D FE solutions with different out-of-plane wavenumbers. For each 2-D FE solution, both the water and the sediment domain were composed of triangular meshes with the maximum element size of 1/6 acoustic wavelength. In contrast, the elements in the rough surface region, around water/seabed interface and the source position were ten times denser (Isakson and Chotiros, 2011; Qing *et al.*, 2019). The physical domain was truncated by a perfectly matched layer which was composed of a mapping mesh of ten layers. For the case of the elastic seabed, the acoustic-solid interaction module was used to couple the acoustic pressure and the solid mechanics domains and establish the acoustic-solid boundary. The geometry and mesh for 2-D FE model can be seen in Fig. 4(b). For both the LIFE model and the ESM-TSM, the segmented integration scheme was performed with 2048 evaluations of 2-D components divided into eight subintervals. In each subinterval, 256 Chebyshev quadrature nodes are required. The suggested parameters for the segmented integral scheme are discussed in Appendix B which also shows a comparison between the proposed segmented integral scheme and the CDF scheme. It should be noted that, for the calculation at 200 Hz, the LIFE model used 31.7 GB disk space to store all the FE solutions and took 5.5 h to compute the solutions using a laptop with i7 8750H CPU and 16 GB of RAM, while the ESM-TSM did not need to save each 2-D solution individually, and only took 4 min to solve for the source strengths of the equivalent sources. The sound field at an arbitrary position was then easily obtained.

TABLE I. Shallow water wedge parameters.

Parameter	Value
Water depth (in the source plane)	100 m
Slope angle	2.86°
Source depth	4 m
Water density	1024 kg/m^3
Water sound speed	1500 m/s
Seabed denstiy	1941 kg/m^3
Seabed compressional speed	1749 m/s
Compressional wave attenuation	0.9 dB/λ
Seabed shear speed (elastic seabed)	800 m/s
Shear wave attenuation (elastic seabed)	0.4 dB/λ
Wind speed	20 m/s

2. Results for the fluid seabed case

First, the fluid seabed scenario was considered. Before calculating the sound field above the fluid seabed, it is necessary to check the accuracy of the water-seabed Green's function by comparing the reflection coefficient with that obtained from the fitted exponentials. Figure 5 shows the comparison of the exact solution with that obtained from a six term fit at 200 Hz, with the asymptotic term subtracted off. A good agreement between the two results can be seen, indicating that the Green's function calculated by the method of complex images is accurate.

Then, Fig. 6(a) shows a 3-D view of the transmission loss (TL) in five vertical planes at $y = 0$, 500, 1000, 1500, and 2000 m and in the horizontal plane for a receiver depth of 40 m at 200 Hz. In the vertical planes, modal cut-off behaviour and scattering features can be seen. The change of the interference pattern along the y-axis indicates the presence of the out-of-plane scattering. Since the transmission into the sediment is absent in the Green's function, the sediment field is not shown in Fig. 6(a). However, it is possible to extend ESM-TSM to the sediment field by introducing the transmission coefficient or by calculating the Green's function using other methods. Figure 6(b) plots the horizontal plane shown in the 3-D plot. Clear interference

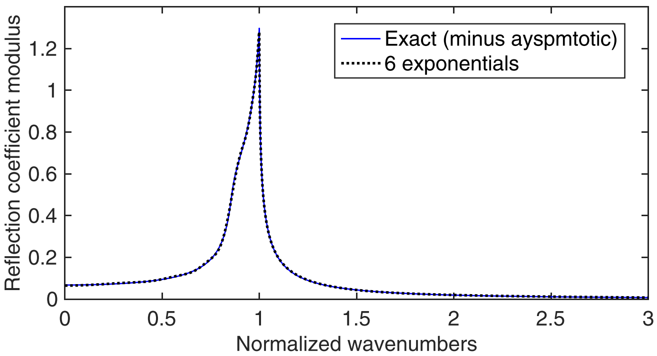

FIG. 5. (Color online) Reflection coefficient modulus for a fluid seabed as a function of wavenumber normalised by $\omega/1500$ (black densely dotted line) compared with the exacted reflection coefficient (blue solid line) at 200 Hz. The asymptotic term has been substracted off.

patterns can be observed for spatial regions far away from the source, with the apparent "elongated" scattering features due to the interaction with sound scattered from the surface roughness. Such a focusing phenomenon can be seen by Smith (2012) and Choo *et al.* (2016).

Figures 7(a) and 7(b) compare the TLs calculated using the LIFE model and the ESM-TSM for a receiver depth of 40 m in the $y = 0$ m plane and in an oblique plane with an azimuth angle of 45° to the x-axis. Excellent agreement between the LIFE model and the ESM-TSM can be seen overall. The root mean square difference of less than 0.2 dB over the whole range for the planes shown indicates the accuracy of the ESM-TSM.

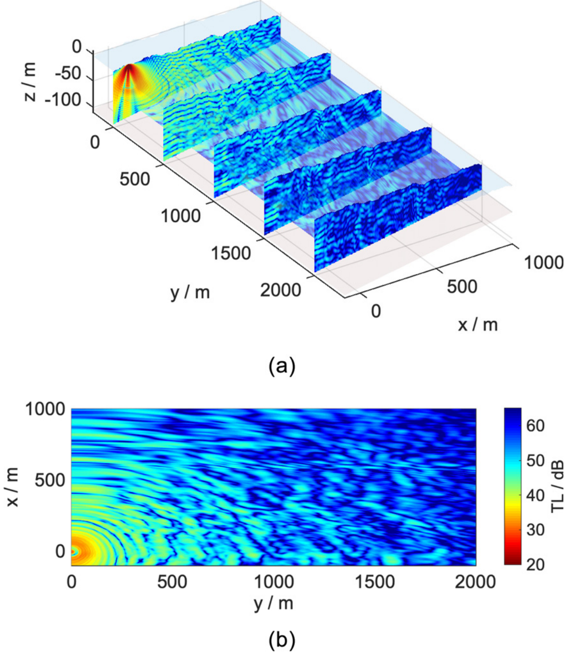

FIG. 6. (Color online) (a) A 3-D view of the propagation in the shallow water wedge for 200 Hz calculated by the ESM-TSM with a horizontal slice for a receiver depth of 40 m and five vertical slices at $y = 0$, 500, 1000, 1500, 2000 m. (b) Sound field calculated by the ESM-TSM in the horizontal plane at a depth of 40 m. The source depth is 4 m.

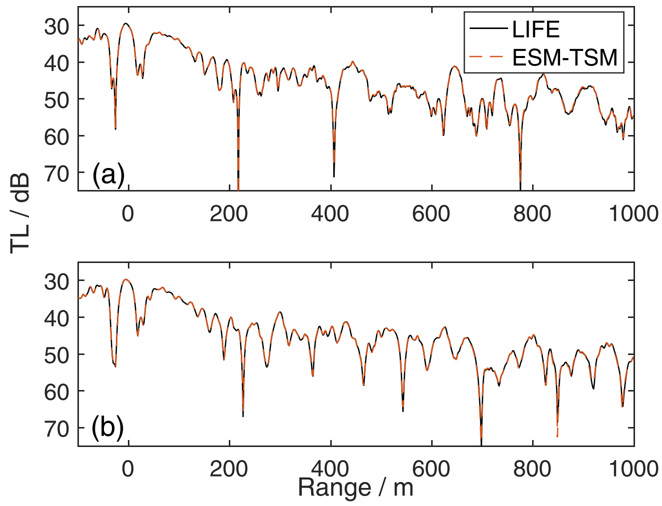

FIG. 7. (Color online) Comparison of the TL calculated by the LIFE model(black solid line) and the ESM-TSM (red dashed line) in (a) the $y = 0$ m plane, (b) an oblique plane with an azimuth angle of 45° to the x-axis, for a receiver depth of 40 m at 200 Hz.

3. Results for the elastic seabed case

Unlike the fluid seabed, the exponential fit for the elastic seabed is more complicated due to the presence of the Scholte pole. Although a weighted fit proposed by Fawcett (2000) is utilised here to improve the robustness, the fitted result is still strongly affected by initial values selected for the nonlinear fit. In this paper, the initial values were set equal to the fitted parameters for the fluid scenario with the same compressional speed and density. Figure 8 shows a comparison of the exact reflection coefficient with the results of the fitted exponential method using the fluid fit parameters as the initial values at 200 Hz. Similar results using zeroes as the initial values are also shown. Apparent singularities can be seen in the exact reflection coefficient, with the most significant peak representing the Scholte pole. By selecting the fluid fit parameters as the initial values, the reflection coefficient result agrees with the exact solution very well for low wavenumber and passes smoothly through the Scholte pole. In contrast, the result of the fit using zeroes

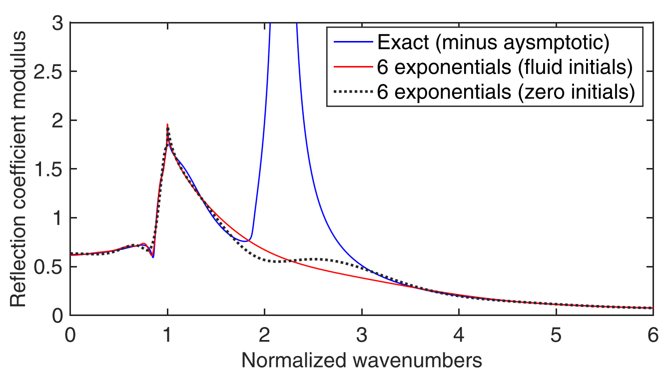

FIG. 8. (Color online) The comparisons of the exact reflection coefficient for an elastic seabed (blue solid line) with the results of the fitted exponential method using the fluid fitted parameters (red dashed line) and zeroes (black densely dotted) as the initial values at 200 Hz.

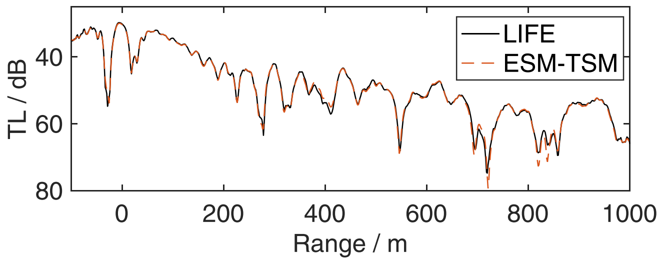

FIG. 9. (Color online) Comparison of the TL calculated by the LIFE model (black solid line) and the ESM-TSM (red dashed line) for an elastic seabed and an oblique plane at an azimuth angle of 45° to the x-axis, for a receiver depth of 40 m at 200 Hz.

as initial values shows an oscillatory fluctuation through the Scholte pole. This means that a more accurate and robust fit can be obtained by the fluid fit parameters as the initial values.

The TL was calculated in the same oblique plane and receiver depth, as shown in Fig. 7(b) for the case of an elastic seabed. The excellent agreement with the LIFE model, shown in Fig. 9, confirms the accuracy of the ESM-TSM for an elastic seabed. A comparison between the case of fluid and elastic seabed for the TL in the $y=0$ plane is shown in Fig. 10(a). The elastic seabed results in greater TL, especially after 400 m, and this is due to the compressional-to-shear wave conversion at the water/seabed interface accompanied by the shear wave attenuation. This greater loss can also be observed in the horizontal plane for a receiver depth of 40 m in Fig. 10(b) by comparison with that shown in Fig. 6(b).

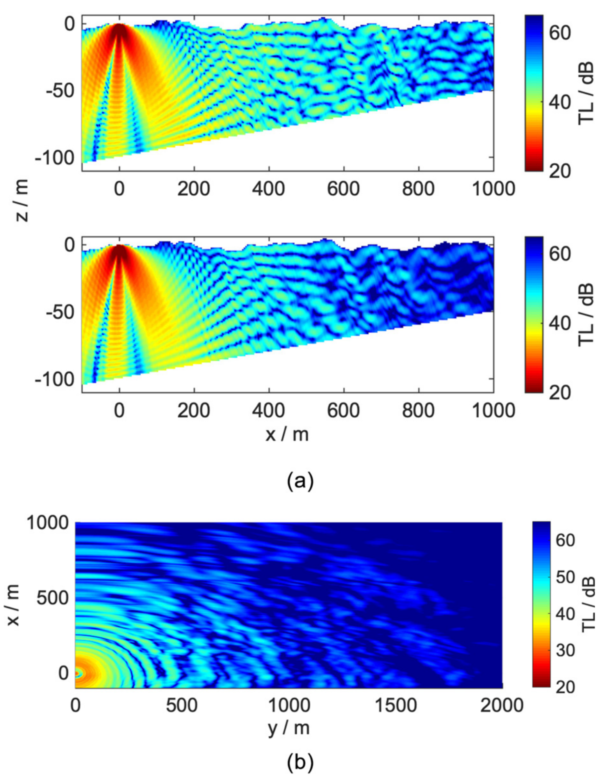

FIG. 10. (Color online) (a) A sound field comparison between the case of fluid seabed (upper plot) and elastic seabed (lower plot) in the $y=0$ plane. (b) Sound field in the horizontal plane at a depth of 40 m above an elastic seabed.

4. Ensemble averaging study

In order to demonstrate the effects of the rough scattering, ensemble average fields for three different wind speeds (10, 15, and 20 m/s) were calculated by performing 50 different implementations of the rough surface for each wind speed at 200 Hz. In this section, only the fluid seabed was considered and the coherent and incoherent field are defined by

$$\begin{cases} p_{coh} = |\langle p \rangle|, \\ p_{incoh} = \sqrt{\langle |p|^2 \rangle - |\langle p \rangle|^2}, \end{cases} \tag{22}$$

where p is the sound pressure from each implementation and $\langle \bullet \rangle$ represents the ensemble average. In order to avoid the situation that the source could be above rough surfaces during the Monte Carlo simulations, the source was set to be 10 m below the surface in this case. Figure 11 illustrates the coherent (upper row) and incoherent (lower row) field as a function of x in the plane at $y=0$ m, and as a function of y in the plane at $x=0$ m for a receiver depth of 40 m. In order to display the effects of rough scattering, the flat surface scenario is also given in the upper row of Fig. 11. It can be seen that, as the wind speed increases, the coherent field overall decreases by up to 10 dB, tending to show similar but smaller fluctuations than those for a flat surface. The greater surface roughness, driven by the higher wind speed, enhances the scattering, especially for situations where the wavelength is smaller than the average wave height. The coherent component can be considered as the lossy specular reflection that reduces in amplitude as the scattering becomes stronger. The non-specular reflection, on the other hand, can be considered as the incoherent field, both in-plane and out-of-plane. Therefore, the incoherent field will show the opposite behaviour to the coherent field as the wind speed increases, which can be observed in Fig. 11.

5. Pulse propagation in the shallow water wedge with a rough surface and fluid seabed

The 3-D propagation of a pulse in the shallow water with a transversely symmetric rough surface is demonstrable and implementable owning to the high numerical efficiency of the ESM-TSM. This helps explain how the out-of-plane scattering arises and may be useful for modelling 3-D shallow water reverberation. The pulse propagation was investigated in the shallow water wedge with the same parameters as used in Sec. III B 2 for the source placed at a depth of 4 m. The time-domain solution was calculated using Fourier synthesis. First, the frequency response was calculated for each frequency, and then the inverse Fourier transform was used to obtain the pulse response. In our case, the source spectrum was centred at 250 Hz, covering the

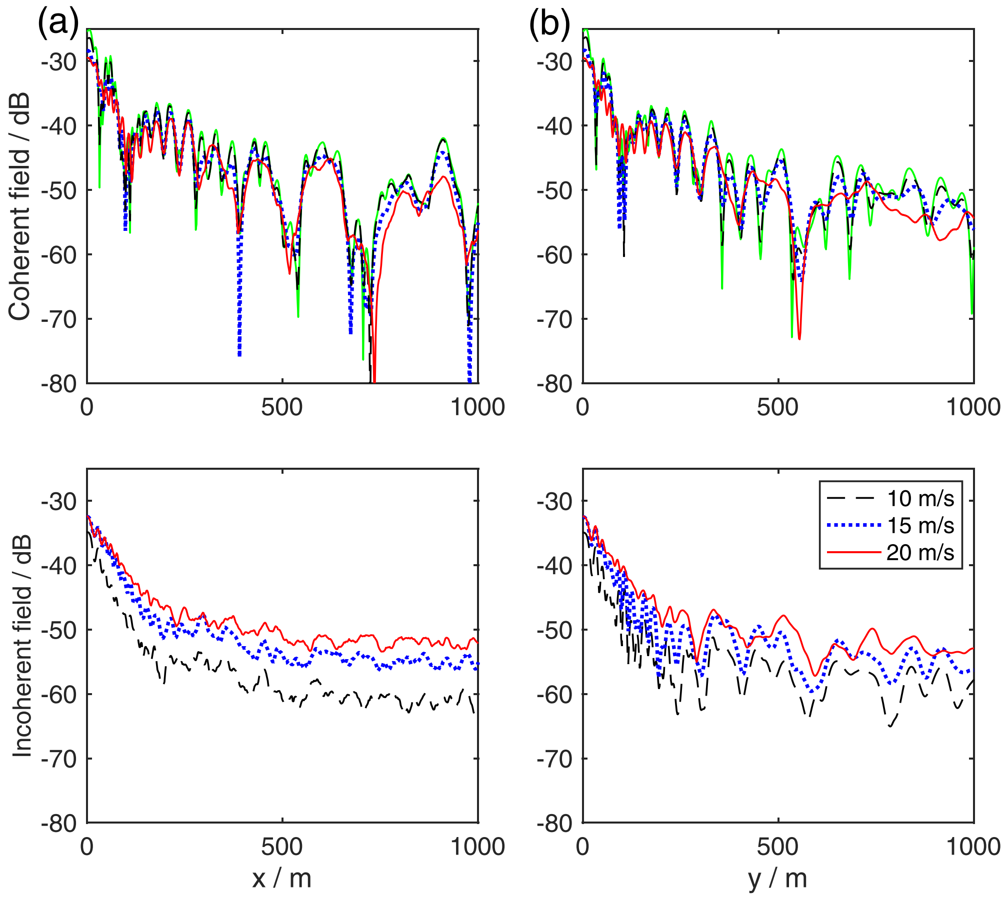

FIG. 11. (Color online) Ensemble averages of the fields for rough surfaces corresponding to wind speeds of 10 m/s (black dashed line), 15 m/s (blue densely dotted line), and 20 m/s (red solid line) at 40 m depth in the: (a) $y=0$ m plane, (b) $x=0$ m plane at 200 Hz. The upper and lower plots show the coherent and incoherent field, respectively. The field for a flat surface is shown as the green solid line that is absent in the lower row due to the zero incoherent field for the flat surface scenario.

frequency range 210–290 Hz. A Tukey window was used as the weighting function in the frequency domain. The frequency interval was selected as $c/2L$, where L was the propagation range. Figure 12 shows the pulse propagation within 600 m with three vertical planes ($y=0$, 300, and 600 m) and a horizontal plane ($z=10$ m). The first bottom bounce scattered by the surface can be seen at $t=0.1477$ s with the apparent "elongated" pattern in the horizontal plane resulting from the transversely symmetric rough surface. This demonstrates how sound is scattered out-of-plane. Similar out-of-plane scattering occurs for subsequent times, caused by the bottom-surface-bottom and bottom-surface-bottom-surface-bottom bounce at $t=0.2462$ s and $t=0.3446$ s, respectively. More details can be found in the movie attached in the supplementary document.[1]

IV. CONCLUSIONS

This paper has demonstrated a propagation model capable of calculating the 3-D scattering from transversely symmetric rough surfaces in both shallow and deep water. The 3-D sound field was obtained by integrating an assembly of 2-D transformed fields with different out-of-plane wavenumbers through a cosine transform. In each 2-D solution, the ESM has been utilised, incorporating a 2-D complex image method under a rotated coordinate system that is capable of calculating the water/seabed half-space Green's function accurately for shallow water wedges. A segmented integral scheme that combines the CDF discretization and the Clenshaw-Curtis quadrature rules is utilised to treat the oscillatory integral accurately using relatively few 2-D solutions. The proposed method has been validated by comparison with a 3-D Helmholtz-Kirchhoff method for a deepwater case with a corrugated sea surface. Simulations were also compared with a longitudinally invariant finite element (LIFE) model in a shallow water wedge for both a fluid and an elastic seabed; the results validate the accuracy of the ESM-TSM. Initial Monte Carlo simulations have been performed to demonstrate the versatility of the technique for showing rough scattering effects. A 3-D pulse propagation has also been demonstrated using the ESM-TSM in the shallow water wedge to understand the out-of-scattering effect visually. The main advantages of the demonstrated approach are high numerical efficiency and easy numerical implementation; desired field points can be calculated without solving the whole physical domain, which enables the multiple implementations required by studies of surface scattering to be performed at a reasonable computational cost. This work can be further applied to research on the rough surface scattering effect on

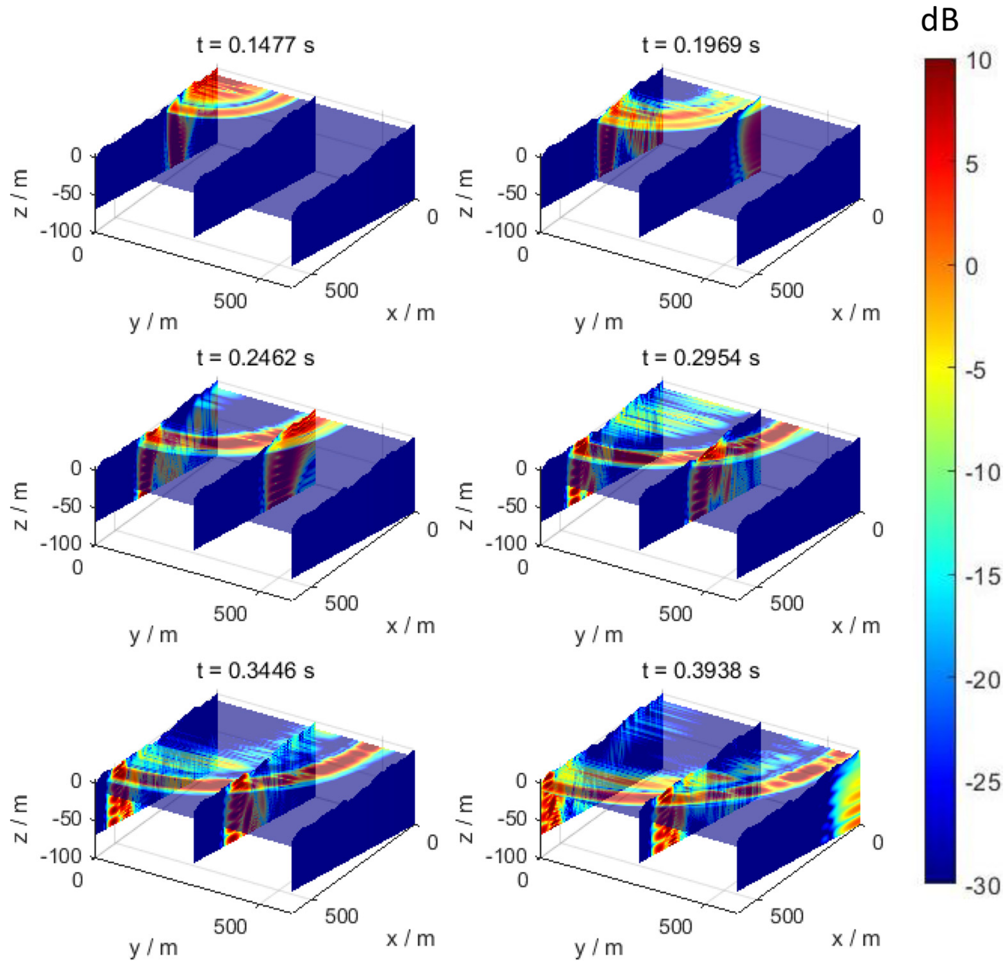

FIG. 12. (Color online) Time evolution of pulse in the shallow water wedge with a rough surface. Times correspond to the following: (a) 0.1477 s, (b) 0.1969 s, (c) 0.2462 s, (d) 0.2954 s, (e) 0.3446 s, (f) 0.3938 s. The *x*-, *y*-, and *z*-axis represent the propagation range, transverse range and depth in *m*, respectively.

URN measurements, and further studies will investigate the extension of the model to a sound refractive medium.

ACKNOWLEDGMENTS

This work was conducted when the first author was on a study visit to the University of Southampton, funded by the Chinese Scholarship Council. This work was also supported by the National Natural Science Foundation of China under Grant No. 11674074. The authors acknowledge associated support services at the University of Southampton in the completion of this work.

APPENDIX A: DETERMINATION OF THE NUMBER OF EQUIVALENT SOURCES

The determination of the number of equivalents sources is discussed in this appendix. To do this, the percentage error has been defined using

$$Percentage\,Error = \frac{|\boldsymbol{P}_{LIFE} - \boldsymbol{P}_{ESM}|_2}{|\boldsymbol{P}_{ESM}|_2} \times 100\%, \quad \text{(A1)}$$

where $\boldsymbol{P}_{LIFE}$ and $\boldsymbol{P}_{ESM}$ were the pressure vectors calculated using the LIFE and the proposed model along the same line shown in Fig. 7(a), and $|\bullet|_2$ represents the two-norm of the vectors. Figure 13 shows the percentage error as a function of the ratio of the wavelength λ to the element length Δ between adjacent equivalent sources along the conformal surface. It can be seen that the error rapidly reduces to around 3.6% after the λ/Δ ratio exceeds 3, which indicates that both the sampling of the incident pressure on the surface and the distribution of equivalent sources require at least approximately three points per wavelength. This result coincides with an equivalent of the Nyquist criterion for sampling waveforms (Holland and Nelson, 2013). Also, this indicates that the rule for determining the number of equivalent sources in this paper is reasonable to ensure accuracy.

APPENDIX B: PARAMETER DETERMINATION FOR THE SEGMENTED INTEGRAL SCHEME

The dependence of the integral accuracy on the segmented integral parameters was investigated for the fluid seabed scenario, and the results were compared with those from the CDF discretisation scheme. The conclusions are also appropriate to the elastic scenario. Both integral schemes were evaluated for 2048 k_y values. For the

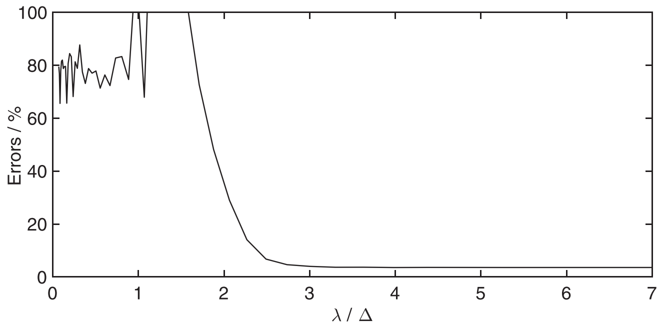

FIG. 13. The percentage error as a function of λ/Δ.

segmented integral scheme, the 2048 values of k_y were divided into 2, 8, or 32 subintervals, and correspondingly there were 1024, 256, and 64 Chebyshev discretisation points in each subinterval. Figure 14 shows the results from the CDF scheme and the segmented integral schemes with different subintervals in the $x = 0$ m plane for a receiver depth of 40 m. It can be seen that the CDF scheme provides the worst convergence once the transverse range exceeds 600 m, while the segmented integral schemes show better performance with the smoothest result obtained by dividing k_y into eight subintervals. This indicates the effectiveness of the segmented integral scheme for large transverse range propagation. Also, the result with two subintervals becomes oscillatory after 1000 m, while that with 32 subintervals remains stable until 1400 m but with significantly larger fluctuations for further transverse ranges. It is known that the Chebyshev quadrature nodes have a decreasing step towards the boundaries of the intervals while the kernel contains the main information and has oscillatory nature away from the boundaries. Very small subintervals fail to capture the main information of the kernel and therefore induce some errors. On the other hand, insufficient quadrature nodes in each subinterval cannot evaluate the integral correctly owing to the rapidly changing nature of the kernel. This suggests that increasing the quadrature nodes is a preferable approach to obtaining an accurate result with relatively few k_ys rather than increasing the number of subintervals. For instance, for more complicated kernels (higher frequencies or more complicated environment

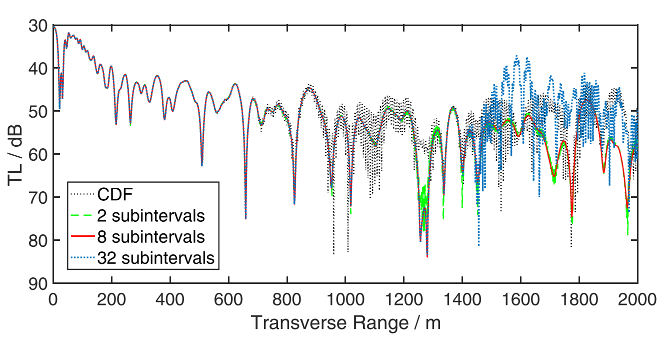

FIG. 14. (Color online) Comparison of the result from the CDF discretisation (black dotted line) with those from the segmented integral scheme with 2 (green dashed line), 8 (red solid line), and 32 (blue dotted line) subintervals, respectively, in the $x = 0$ m plane for a receiver depth of 40 m.

model), the number of subintervals can follow the robust value of 8 used in this paper, but with more Chebyshev quadrature nodes within each subinterval.

[1]See supplementary material at https://doi.org/10.1121/10.0001522 for movies of the pulse propagation for both the rough surface and flat surface scenarios.

Audoly, C., and Meyer, V. (**2017**). "Measurement of radiated noise from surface ships—Influence of the sea surface reflection coefficient on the Lloyd's mirror effect," in *Proceedings of ACOUSTICS*, Vol. 19.

Ballard, M. S. (**2013**). "Three-dimensional acoustic propagation under a rough sea surface," Proc. Mtgs. Acoust. **19**, 070077.

Ballard, M. S., Goldsberry, B. M., and Isakson, M. J. (**2015**). "Normal mode analysis of three-dimensional propagation over a small-slope cosine shaped hill," J. Comput. Acoust. **23**(03), 1550005.

Choo, Y., Song, H., and Seong, W. (**2016**). "Numerical study of three-dimensional sound reflection from corrugated surface waves," J. Acoust. Soc. Am. **140**(4), 2290–2296.

Collins, M. D., Coury, R. A., and Siegmann, W. L. (**1995**). "Beach acoustics," J. Acoust. Soc. Am. **97**(5), 2767–2770.

Deane, G., and Buckingham, M. (**1993**). "An analysis of the three-dimensional sound field in a penetrable wedge with a stratified fluid or elastic basement," J. Acoust. Soc. Am. **93**(3), 1319–1328.

Fawcett, J. A. (**2000**). "Complex-image approximations to the half-space acousto-elastic Green's function," J. Acoust. Soc. Am. **108**(6), 2791–2795.

Fawcett, J. A. (**2003**). "A method of images for a penetrable acoustic waveguide," J. Acoust. Soc. Am. **113**(1), 194–204.

Golub, G. H., Hansen, P. C., and O'Leary, D. P. (**1999**). "Tikhonov regularization and total least squares," SIAM J. Matrix Anal. Appl. **21**(1), 185–194.

Holland, K., and Nelson, P. (**2013**). "The application of inverse methods to spatially-distributed acoustic sources," J. Sound Vib. **332**(22), 5727–5747.

Isakson, M. J., and Chotiros, N. P. (**2011**). "Finite element modeling of reverberation and transmission loss in shallow water waveguides with rough boundaries," J. Acoust. Soc. Am. **129**(3), 1273–1279.

Isakson, M. J., and Chotiros, N. P. (**2014**). "Finite element modeling of acoustic scattering from fluid and elastic rough interfaces," IEEE J. Ocean. Eng. **40**(2), 475–484.

Isakson, M. J., Goldsberry, B., and Chotiros, N. P. (**2014**). "A three-dimensional, longitudinally-invariant finite element model for acoustic propagation in shallow water waveguides," J. Acoust. Soc. Am. **136**(3), EL206–EL211.

Koopmann, G. H., Song, L., and Fahnline, J. B. (**1989**). "A method for computing acoustic fields based on the principle of wave superposition," J. Acoust. Soc. Am. **86**(6), 2433–2438.

Lusseau, D., Bain, D. E., Williams, R., and Smith, J. C. (**2009**). "Vessel traffic disrupts the foraging behavior of southern resident killer whales Orcinus orca," Endang. Spec. Res. **6**(3), 211–221.

Mullor, R. S., Moreno, A., and Palomo, P. B. (**2013**). "Identification and evaluation of the uncertainties in the current measurement standards, within the framework of AQUO project," in *The 3rd International Conference on Advanced Model Measurement Technology for the EU Maritime Industry*, Gdansk, Poland.

Nowacek, S. M., Wells, R. S., and Solow, A. R. (**2001**). "Short-term effects of boat traffic on bottlenose dolphins, *Tursiops truncatus* in Sarasota bay, Florida," Marine Mammal Sci. **17**(4), 673–688.

Pereira, A., Antoni, J., and Leclere, Q. (**2015**). "Empirical Bayesian regularization of the inverse acoustic problem," Appl. Acoust. **97**, 11–29.

Qing, X., White, P. R., Leighton, T. G., Liu, S., Qiao, G., and Zhang, Y. (**2019**). "Three-dimensional finite element simulation of acoustic propagation in spiral bubble net of humpback whale," J. Acoust. Soc. Am. **146**(3), 1982–1995.

Rodríguez, A. M., Mullor, R. S., Palomo, P. B., Baudin, E., and Lamaison, V. (**2015**). "New European underwater noise measurement standard developed in the AQUO project," in *OCEANS 2015-Genova*, IEEE, pp. 1–6.

Rosenberg, A. P. (**1999**). "A new rough surface parabolic equation program for computing low-frequency acoustic forward scattering from the ocean surface," J. Acoust. Soc. Am. **105**(1), 144–153.
Simon, B., Isakson, M., and Ballard, M. (**2018**). "Modeling acoustic wave propagation and reverberation in an ice covered environment using finite element analysis," Proc. Mtgs, Acoust. **33**, 070002.
Smith, K. B. (**2012**). "Field transformational approach to three-dimensional scattering from two-dimensional rough surfaces," J. Acoust. Soc. Am. **131**(6), EL441–EL447.
Thorsos, E. I. (**1990**). "Acoustic scattering from a 'Pierson-Moskowitz' sea surface," J. Acoust. Soc. Am. **88**(1), 335–349.
Thorsos, E. I., Henyey, F. S., Elam, W., Reynolds, S. A., and Williams, K. L. (**2004**). "Modeling shallow water propagation with scattering from rough boundaries," AIP Conf. Proc. **728**, 132–140.
Waldvogel, J. (**2006**). "Fast construction of the Fejér and Clenshaw–Curtis quadrature rules," BIT Numer. Math. **46**(1), 195–202.
Welton, P. (**2012**). "Three dimensional analyses of scattering by pressure-release sinusoidal surfaces," J. Acoust. Soc. Am. **131**(1), 54–68.
Yang, J., and Chow, Y. (**1991**). "Discrete complex images of a three-dimensional dipole above and within a lossy ground," in *IEE Proceedings H (Microwaves, Antennas and Propagation)*, IET, Vol. 138, pp. 319–326.